Dovepress

ORIGINAL RESEARCH

Acidic Environment-Responsive Metal Organic Framework-Mediated Dihydroartemisinin Delivery for Triggering Production of Reactive Oxygen Species in Drug-Resistant Lung Cancer

Xiaojie Yan[1,]*, Xueying Zhao[2,]*, Mingde Fan[3], Wenfu Zheng[4,5], Guanxiong Zhu[6], Bin Li[1], Le Wang[1]

[1]Academician Workstation, Jiangxi University of Chinese Medicine, Nanchang, Jiangxi, People's Republic of China; [2]Department of Transfusion, The Second Hospital, Cheeloo College of Medicine, Shandong University, Jinan, Shandong, People's Republic of China; [3]Department of Neurosurgery, The Second Hospital, Cheeloo College of Medicine, Shandong University, Jinan, Shandong, People's Republic of China; [4]CAS Key Laboratory for Biological Effects of Nanomaterials and Nanosafety, National Center for NanoScience and Technology, Beijing, People's Republic of China; [5]School of Nanoscience and Engineering, University of Chinese Academy of Sciences, Beijing, People's Republic of China; [6]Department of Preventive Dentistry, Affiliated Stomatology Hospital of Guangzhou Medical University, Guangzhou, Guangdong, People's Republic of China

*These authors contributed equally to this work

Correspondence: Le Wang; Bin Li, Academician Workstation, Jiangxi University of Chinese Medicine, Nanchang, Jiangxi, People's Republic of China, Tel/Fax +86-791-86362367, Email wangle@jxutcm.edu.cn; 20010260@jxutcm.edu.cn

Background: Dihydroartemisinin (DHA) has emerged as a promising candidate for anticancer therapy. However, the application of DHA in clinics has been hampered by several limitations including poor bioavailability, short circulation life, and low solubility, significantly restricting its therapeutic efficacy and leading to notable side effects during the treatment.

Purpose: We present DHA-loaded zeolitic imidazolate framework-8 (D-ZIF) with controllable and targeted DHA release properties, leading to enhanced antitumor effects while reducing potential side effects.

Methods: D-ZIF was prepared by one-pot synthesis method using methylimidazole (MIM), $Zn(NO_3)_2 \cdot 6H_2O$ and DHA. We characterized the physical and chemical properties of D-ZIF by TEM, DLS, XRD, FT-IR, and TG. We measured the drug loading efficiency and the cumulative release of DHA in different pH conditions. We evaluated the cytotoxicity of D-ZIF on renal cell carcinoma (RCC786-O), glioma cells (U251), TAX-resistant human lung adenocarcinoma (A549-TAX) cells by CCK8 in vitro. We explored the possible antitumor mechanism of D-ZIF by Western blot. We evaluated the biocompatibility and hemolysis of D-ZIF and explored the in vivo antitumor efficiency in mice model by TUNEL testing and blood biomarker evaluations.

Results: D-ZIF showed rhombic dodecahedral morphology with size of 129±7.2 nm and possessed a noticeable DHA encapsulation efficiency (72.9%). After 48 hours, D-ZIF released a cumulative 70.0% of the loaded DHA at pH 6.5, and only 42.1% at pH 7.4. The pH-triggered programmed release behavior of D-ZIF could enhance anticancer effect of DHA while minimizing side effects under normal physiological conditions. Compared with the free DHA group with 31.75% of A549-TAX cell apoptosis, the percentage of apoptotic cells was approximately 76.67% in the D-ZIF group. D-ZIF inhibited tumor growth by inducing tumor cell apoptosis through the mechanism of ROS production and regulation of Nrf2/HO-1 and P38 MAPK signaling pathways. D-ZIF showed potent effects in treating tumors with high safety in vivo.

Conclusion: This pH-responsive release mechanism enhanced the targeting efficiency of DHA towards tumor cells, thereby increasing drug concentration in tumor sites with negligible side effects. Herein, D-ZIF holds great promise for curing cancers with minimal adverse effects.

Keywords: MOF, drug delivery, controlled release, cancer therapy

Introduction

Cancers especially lung cancer pose a significant threat to human health.[1–3] For a considerable duration, patients facing cancers had limited options for treatment, primarily relying on surgery, radiation therapy, and chemotherapy, either individually or in combination.[4] A significant challenge associated with chemotherapy is the development of drug resistance.[5]

Multi-drug resistance (MDR) in cancer cells, whether intrinsic or acquired, leads to reduced drug absorption and increased drug efflux, representing a substantial obstacle to the therapeutic effectiveness of drugs. In tackling these challenges, nanotechnology-based delivery systems have demonstrated the ability to provide controlled and targeted delivery,[6] thereby enhancing the intracellular availability of drugs and exploring opportunities to overcome MDR.[7] Recently, the active derivatives of traditional Chinese medicine have emerged as cancer therapy candidates.[8–10] Artemisinin, derived from the plant Artemisia annua with a sesquiterpene lactone structure containing a peroxide group, is an antimalarial drug.[11] It was first isolated by Youyou Tu in 1971 and has gained widespread recognition as an effective treatment for malaria.[12,13] In addition to antimalarial effects, artemisinin and its derivatives demonstrate notable anti-tumor effects, which encompass the inhibition of angiogenesis, tumor cell invasion, and metastasis within the tumor microenvironment.[14] Additionally, artemisinin hinders various aspects of tumor progression by inducing ferroptosis in cancer cells and activating pathways associated with apoptosis and autophagy.[15] Dihydroartemisinin (DHA), one of the artemisinin derivatives, provides improved anti-tumor activity in vitro and in vivo.[16] However, the clinical application of DHA has been hindered by challenges such as low solubility, poor bioavailability, resistance induction, and non-specific distribution, primarily due to glucopyranose rings in its chemical structure. Thus, to improve the therapeutic efficiency of DHA, an appropriate drug delivery system is highly needed.

The previously reported delivery systems, such as liposomes,[17–19] polymers,[20–22] and inorganic nanomaterials,[23–26] show great potential for delivering drugs. Liposomes represent an excellent approach for drug delivery, however, only 14 types of liposomal products are currently available on the market.[18] In our previous study, we introduced a novel liposome-based CRISPR/Cas9 delivery system, showcasing significantly high efficiency in treating melanoma.[19] However, these vehicles usually lack active-targeting capability. The microenvironment at the target tumor site can be utilized to initiate drug release from the polymer carrier. Various external or internal stimuli, including temperature, pH, light, electromagnetic fields, enzymes, and hypoxia, are commonly explored as "on-off" switches for drug release. Researchers developed poly(β-aminoester) dendrimers, exhibiting both pH and temperature responsiveness.[27] The emergence of metal-organic frameworks (MOFs) provides a targeted drug delivery system. The porous structure of MOFs significantly improves drug-loading capacity, and the versatility in selecting metal ions and organic ligands allows the creation of MOFs with intrinsic antitumor activities.[28–31] The versatility further enables the development of MOF-drug synergistic systems, sustaining targeted and controlled drug release while reducing drug toxicity, which renders MOFs ideal carriers for intelligent drug delivery.[32] Active-node MOFs can be utilized for chemodynamic therapy and radiotherapy, contributing to the catalytic modulation of tumor microenvironments. Furthermore, MOFs incorporating photosensitizers, chemotherapeutic drugs, and peptides as active linkers demonstrate significance in the treatment of various cancers, particularly those affecting the bone, breast, and colon, which extend to photodynamic therapy, photothermal therapy, stem cell therapy, and immunotherapy.[33] The iron-based MOF has been investigated for the potential in delivering anticancer drugs due to its high biocompatibility, biodegradability, and water stability. MIL-101(Fe) loaded with DHA exhibited significant uptake by tumor-associated macrophages (TAM), effectively addressing the inefficiency of DHA at low concentrations.[34] Fe-TCPP [(4,4,4,4-(porphine-5,10,15,20-tetrayl) tetrakis(benzoic acid)] MOF, featuring a core-shell structure mineralized with $CaCO_3$, prevented DHA leakage during bloodstream transport.[35] Compared to iron-based MOF, zinc-based MOF, such as the zeolitic imidazolate framework (ZIF), possess robust bonds between metal ions (or clusters), granting them unique properties that include the capability to accommodate and safeguard a range of biomolecules, along with the controlled release of drug molecules, ensuring satisfactory biocompatibility. ZIF-DHA nanoparticles exhibited superior anti-tumor therapeutic activity in several ovarian cancer cells, coupled with the suppression of cellular reactive oxygen species production and the induction of apoptotic cell death.[36] Utilizing co-loaded DHA and indocyanine green, a drug delivery system based on ZIF was employed for synergistic chemo-photothermal therapy for cancer cells based on pH/NIR-responsive drug release.[37] Specifically, ZIF-8 emerges as a highly promising candidate for intracellular drug delivery due to its elevated hydrothermal stability, excellent monodispersity, and optimal size conducive to cellular uptake.[38] Our previous work indicated that ZIF-8 could efficiently encapsulate biomolecules, surpassing the encapsulation percentages achieved through conventional methods.[39] However, how to rationally design ZIF8-based nanomaterials for improving tumor delivery efficiency for targeted cancer therapy remains a critical challenge.

Herein, we rationally designed pH-responsive DHA delivery system based on ZIF-8 (abbreviated as ZIF) to develop highly efficient and targeted treatments for lung cancer by harnessing the integrating specific strategies (Figure 1). By loading DHA (abbreviated as D) in the pH-sensitive ZIF, the resulting D-ZIF displays a synergistic cancer therapeutic effect with high biosafety. The pH-responsive release mechanism enhances the targeting efficiency of DHA toward TAX-resistant human lung
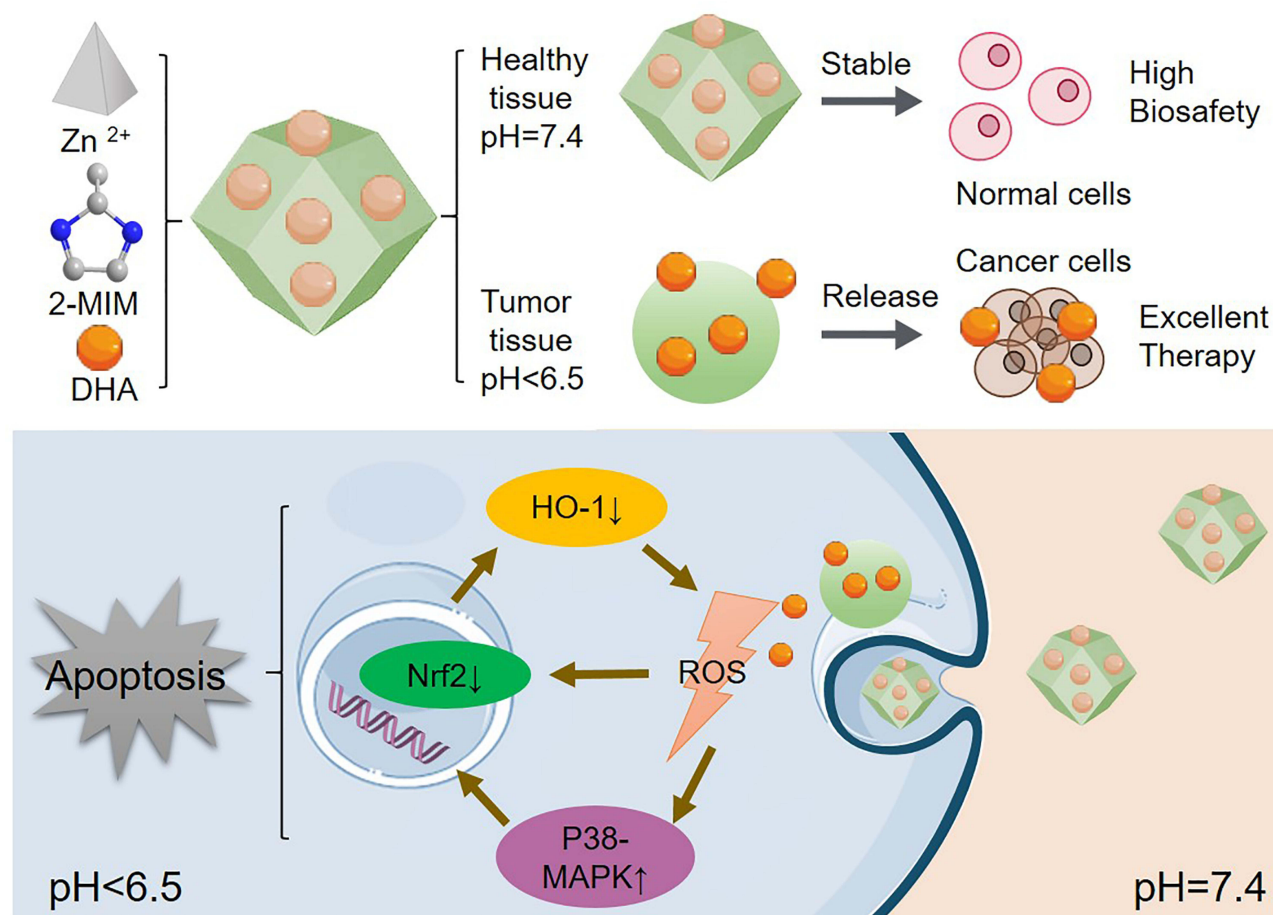
Figure 1 Schematic illustration of the preparation process and antitumor mechanism of D-ZIF as an antitumor agent.

adenocarcinoma (A549-TAX) cells, thereby increasing the drug concentration in tumor sites. This work highlights the potential of utilizing D-ZIF to maximize therapeutic efficiency with negligible side effects in complicated tumor environments and demonstrates a great potential to be utilized as a precise therapeutic strategy for treating lung cancer. In comparison to the above delivery system, our approach is widely applicable and ensures heightened safety. With the enhanced stability, pH responsiveness, and high drug loading capacity, we believe that our approach shows potential for addressing a wide array of drug-resistant diseases, encompassing cancers, heritable diseases, and infectious diseases.

Materials and Methods
Materials
Zinc nitrate hexahydrate ($Zn(NO_3)_2\cdot6H_2O$, 98%, Mw=297.49), dihydroartemisinin (98%, Mw=284.35) and 2-methylimidazole (MIM, 99%, Mw=82.11) were obtained from Aladdin (China). Fetal bovine serum (FBS), Dulbecco's modified Eagle's medium (DMEM), penicillin and streptomycin (PS) were obtained from Gibco (USA). Live/dead cell staining kit was purchased from Abbkine (China). Dino-2-phenylindole (DAPI) was purchased from Solarbio (China). Acridine orange-ethidium bromide (AO-EB) dual staining kit was purchased from Bestbio (China). The reactive oxygen species (ROS) assay kit was purchased from Beyotime (China). Cell proliferation and cytotoxicity assay kit, Annexin V-FITC/PI apoptosis detection kit and TUNEL BrightRed apoptosis detection kit were purchased from Vazyme (China).

Preparation of D-ZIF
We used the optimized synthesis method to prepare ZIF at room temperature according to our previous study.[31] In brief, we mixed the MIM (1000 μg/mL), $Zn(NO_3)_2\cdot6H_2O$ (50 μg/mL) and DHA (20 μg/mL) in water with vigorous stirring (2000 rpm).

After 15 min, DHA-loaded ZIF (D-ZIF) was separated from the dispersion by centrifugation (HeraeusMultifuge X1R, Thermo Fisher Scientific, USA, 15,000 rpm) and rinsed with ultrapure water three times to remove the unreacted reagents and unloaded DHA. We freeze-dried D-ZIF and stored it at −20 °C until further use. Under the same synthetic conditions, we synthesized ZIF as the control group without adding DHA.

Characterization of D-ZIF

We characterized the morphologies and Zeta potential of D-ZIF by a transmission electron microscopy (TEM, Tecnai F30, USA) and a Zetasizer Nano ZS (Malvern Company, England), respectively. We measured the crystal structure and absorption spectra of D-ZIF by X-ray diffraction (XRD, Rigaku Smartlab, Japan) and UV-visible spectrophotometer (UV-2600, Japan). We characterized the chemical compositions and weight-loss of the D-ZIF by a Fourier transform infrared spectroscopy (FT-IR Spectrum One, USA) and Thermogravimeter (TG, TA Q5000IR, USA), respectively. We characterized encapsulation efficiency and drug loading content of DHA through inhibition with NaOH (0.2%) at 50 °C for 30 min and the detected wavelength at 290 nm by the UV-visible spectrophotometer.[40] We detected the drug loading efficiency (LE) using the following equation: Drug loading efficiency (%) = $(M_{total\ drug}-M_{free\ drug})/(M_{total\ drug}) \times 100\%$.

Cell Viability Assay

A549 was obtained from the American Type Culture Collection (ATCC, USA). To develop paclitaxel resistance in the A549 cell line (A549-TAX), we subjected A549 cells to progressively higher concentrations of paclitaxel (NSC125973, Selleck, Shanghai, China) ranging from 20 to 120 nM, employing an intermittent exposure method as described in a previous study.[41] We cultured cells in DMEM (10% FBS and 1% PS) at 37 °C with 5% CO_2. Before experimenting, the cells were cultured in medium without any drugs for a minimum of two weeks. For the cytotoxicity assessment, we seeded the A549-TAX cells (5×10^3 cells/96-well plate) with different concentrations of free DHA, ZIF, and D-ZIF (1, 5, 10, 20, and 50 μg/mL for DHA and corresponding concentrations for ZIF) for 24 h and added the cell counting kit-8 (CCK8) reagent (10 μL) to each well. After 1 h incubation, we measured the absorbance values using a microplate reader (Emax Precision, USA) at 450 nm to calculate cytotoxicity. Cell viability (%) = $(A_x-A_0)/(A_y-A_0) \times 100\%$, where A_y was the absorbance of the negative control group, A_x was the absorbance of the experimental group, A_0 was the absorbance of the blank control group.

Reactive Oxygen Species (ROS) Detection

To investigate the generation of ROS, we seeded the A549-TAX cells (1×10^5 cells/well) and treated the cells with free DHA, ZIF, and D-ZIF for 6 h in a cell culture plate, respectively. We diluted Dichlorodihydrofluorescein diacetate (DCFH-DA) with the DMEM medium at a ratio of 1:1000 dilution. After washing the treated cells with PBS twice, we added 10 μL of the diluted DCFH-DA to each well and incubated the cells for 20 min. After removing the any residual DCFH-DA and rinsed cells twice, we measured the 2',7'-dichlorofluorescein (DCF) fluorescence (excitation, 488 nm; emission, 525 nm) using a fluorescence microscope (Olympus IX73, Japan).

Flow Cytometry and Cell Staining

For flow cytometry analysis, we treated A549-TAX, renal cell carcinoma (RCC786-O), and glioma cells (U251) (2×10^5 cells/12-well plate) with free DHA, ZIF, and D-ZIF at a concentration of 5 μg/mL (for DHA), or D-ZIF at concentrations of 1, 5, and 10 μg/mL (for DHA) for 24 h. U251 and RCC786-O cell lines were purchased from Procell (Wuhan, China). We measured the 2',7'-dichlorofluorescein (DCF) fluorescence using flow cytometry to detect ROS. Apoptosis detection was performed using flow cytometry (CytoFLEX) based on the instructions provided with the Annexin V-FITC/PI Apoptosis Detection Kit. To observe morphological changes in cells, we cultured A549-TAX cells in a 24-well plate and subsequently treated them with free DHA, ZIF, and D-ZIF at a concentration of 5 μg/mL (for DHA) for 12 h. After rinsing the cells with PBS twice, we stained the treated cells by a mixture of acridine orange/ethidium bromide (AO-EB, Bestbio, China) for 20 min at 4 °C. To examine the morphology of apoptotic cells, fluorescence microscopy (BX53, Olympus, Japan) was employed.

Western Blot

We lysed the treated A549-TAX cells by a lysis buffer (Solarbio, China) with a protease inhibitor. We collected the protein samples in the supernatants after centrifugation (12,000 rpm 15 min). We loaded 10 μg protein samples on the 10–12% polyacrylamide gels for electrophoresis and subsequently transferred them to PVDF membranes (EMD Millipore, Billerica, MA, USA). We incubated the membranes with primary antibodies at 4 °C. The primary antibodies used in this study included Nrf2, HO-1, caspase-3, p-ERK, ERK, p-P38, P38, and β-actin. These antibodies were diluted at a ratio of 1:1000. Following the primary antibody incubation, we incubated membranes with secondary antibodies. We applied ECL Western Blotting Detection Reagent to detect the bands. To quantify the band intensity, we used Image J software.

Toxicity Evaluation

To assess the cytotoxicity of the ZIF delivery system, we conducted in vitro tests on A549-TAX cells by testing the cell viability. We treated the A549-TAX cells (5×10^3 cells/96-well plate) with ZIF at concentrations of 40, 80, 160, 320, and 640 μg/mL for 24 h. We added the –CCK8 (10 μL) to each well and measured the optical density using a microplate reader at 450 nm to calculate cytotoxicity. We also treated A549-TAX cells (2×10^5 cells/well) with ZIF (40, 80, and 160 μg/mL) to evaluate the morphological change of cells by a microscope (CKX53, Olympus, Japan). Additionally, we examined the biocompatibility of ZIF and D-ZIF using a hemolysis assay. We collected fresh rat red blood cells by centrifuging them at 1500 rpm for 15 min. We washed the collected cells three times with PBS and added different concentrations of ZIF (40, 80, 160, and 320 μg/mL), DHA and D-ZIF (5, 10, 20, and 50 μg/mL) in solution with a total volume of 400 μL. After 3h incubation, the mixed solution was subjected to centrifugation at 1500 rpm for 5 min. The optical density of the supernatant was then measured at a wavelength of 567 nm (OD_{567nm}) using a microplate reader. All experiments were performed three times to ensure reliability and consistency.

Animal Model and Antitumor Activity Evaluation in vivo

For the animal study, BALB/c nude mice (6 weeks, female) were accommodated in the SPF-grade Animal Experimental Center of the Second Hospital of Shandong University. The animal procedures were conducted following the ethical standards approved by the Ethics Committee of the Second Hospital of Shandong University (Ethical Approval Number KYLL-2022-365). We injected 1×10^7 A549-TAX cells into the mice flanks subcutaneously. The mice were randomly divided into four groups: control, DHA (5.0 mg/kg), ZIF, and D-ZIF (equivalent to 5.0 mg/kg DHA). The calculation of tumor volumes was performed using the formula: V = Width × Width × 1/2 × Length. When the tumor volume reached approximately 100 mm³, we administered different agents (DHA, ZIF, and D-ZIF) into the tumor every 2 days for 6 injections, setting PBS-treated group as a control. We recorded the body weight of the mice at two-day intervals. The tumors were excised, weighed, and photographed at the 13th day for the following evaluation.

Antitumor Mechanism Evaluation in vivo

To detect apoptosis, we first fixed tumor sections by 4% paraformaldehyde and then rinsed the sliced specimens twice with PBS. We used Triton X-100 (0.2%) for permeabilization. We treated the sections with 50 μL TUNEL working solution according to the TUNEL BrightRed Apoptosis Detection Kit. We detected red fluorescence at 620 nm under a confocal laser scanning microscopy to analyze histological characteristics. We sectioned the tissues into 4 μm thickness and stained them with hematoxylin and eosin. We scanned the sections with a NanoZoomer S60 digital pathology scanner (NanoZoomer S60, Hamamatsu, Japan) to observe the pathological structure. To assess hepatic or renal toxicity, we collected the mice blood samples and subsequently centrifuged the samples to collect serum. We detected the blood parameters by a blood automatic biochemical analyzer (Seamaty, China).

Statistical Analysis

We performed the experiments at least three independent replicates. The data were presented as mean ± standard deviation (Mean ± SD). One-way or two ways analysis of variance (ANOVA) was employed to evaluate significance among multiple groups, with a *P*-value < 0.05 indicating statistical significance.

Results and Discussion

Characterization of D-ZIF

We obtained ZIF8 NPs (abbreviated as ZIF) using the one-pot synthesis method to carry DHA. With the mixture of methylimidazole (MIM) and DHA as precursor and zinc as the additive, DHA-loaded ZIF (D-ZIF) could be prepared by coordination between Zn^{2+} and MIM. The Zeta potential values for pure ZIF and D-ZIF was +29.8 and −9.3mV, respectively (Supplementary Data, Figure S1A), indicating the successful establishment of the delivery system. Both ZIF and D-ZIF showed rhombic dodecahedral morphology with size of 112±9.1 nm and 129±7.2 nm respectively under transmission electron microscopy (Figure 2A). Also, ZIF and D-ZIF exhibited uniformity without detectable aggregation under dynamic light scanning (DLS) (Figure 2B), demonstrating excellent dispersibility and stability. The loading of DHA did not lead to a significant increase in the size of ZIF, indicating that the incorporation of DHA had no significant impact on the structure of the delivery system. Fourier transform infrared (FTIR) spectroscopy showed that new absorption peaks around 500–1500 cm^{-1} appeared in the sample of D-ZIF compared with ZIF, indicating the successful load of DHA in the ZIF delivery system (Figure S1C). This is helpful for the protection of DHA and enabling its desired biological effects in complex physiological environments. We characterized the crystallinity of ZIF and D-ZIF by X-ray diffraction. The bare ZIF exhibited characteristic peaks at 7.3°, 10.3°, 12.7°, 14.8°, 16.4°, and 18.0°, revealing the (110), (200), (211), (220), (310), and (222) of framework structure of Zn corresponding to JCPDS #04-0784, which confirms structural integrity of ZIF-8 (Figure 2C). We characterized the load capability of D-ZIF. UV-vis absorption analysis showed a high loading efficiency of 72.9% for DHA. We also quantified DHA loading content in D-ZIF by thermal gravimetric analysis (TGA) under a nitrogen gas flow. The removal of DHA molecules from D-ZIF showed
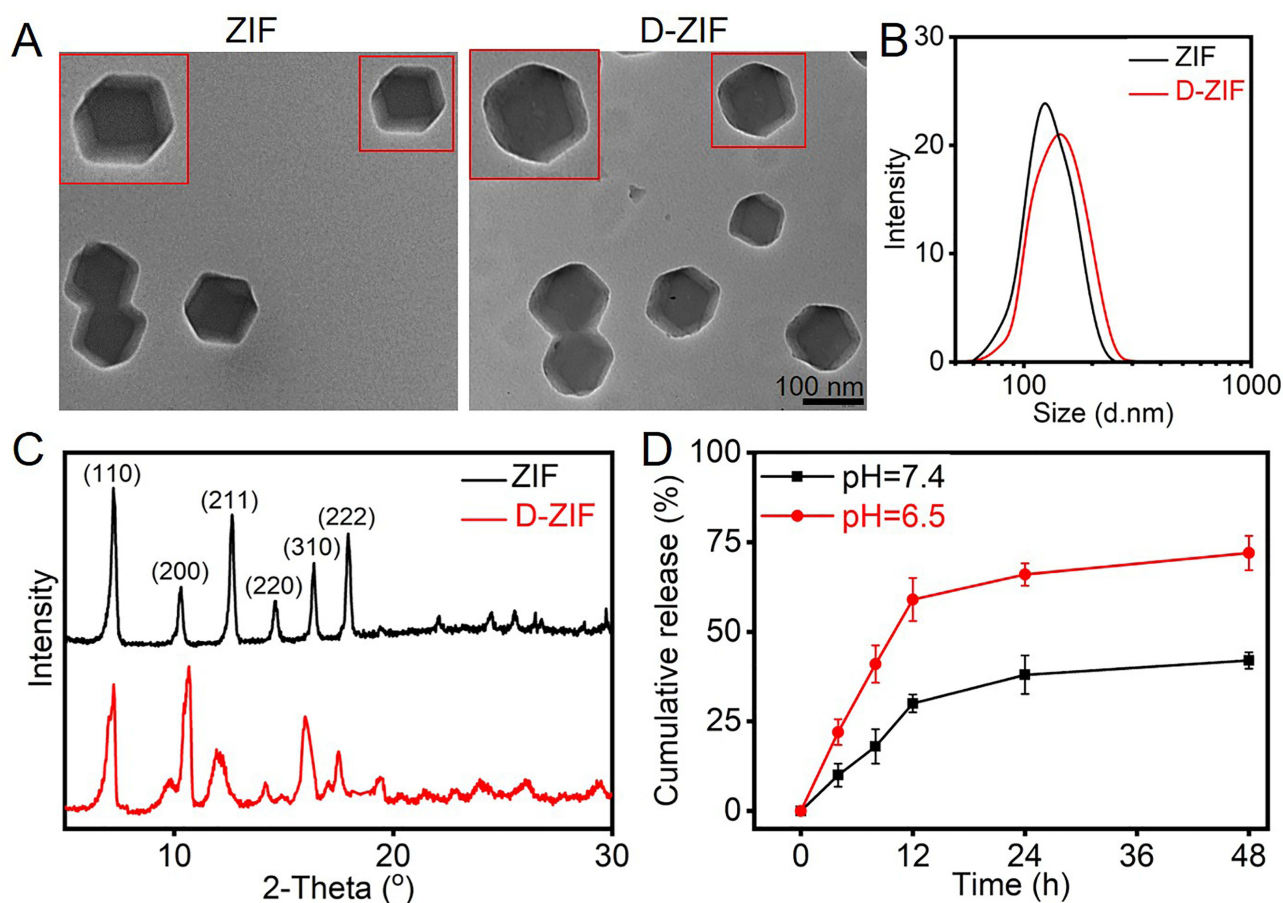

Figure 2 Characterization of ZIF and D-ZIF. (**A**) TEM images of ZIF and D-ZIF. Single NPs are highlighted in red frames. Scale bar, 100 nm. (**B**) The size distribution analysis of ZIF and D-ZIF by DLS. (**C**) The crystallinity of ZIF and D-ZIF by XRD. (**D**) Cumulative release of DHA in different pH values at 48 h for D-ZIF.

approximately 13.8 wt% of weight loss, which is consistent with the data in UV-vis analysis (Figure S1B). This system effectively improves the bioavailability of DHA by incorporating it into ZIF.

A desirable characteristic of the delivery system should possess stability under normal physiological situations and biodegradability in acidic tumor conditions. To investigate the release behavior of D-ZIF in response to pH change, we incubated D-ZIF in PBS at pH values of 6.5 and 7.4, respectively. ZIF exhibited obvious structural collapse and partially degraded at pH 6.5 after 24 h (Figure S2). The pH-triggered programmed release behavior of D-ZIF could enhance the DHA anticancer effect. We calculated and plotted the released amount of DHA by measuring OD_{290nm} at different time points. DHA showed a faster release rate in pH 6.5 than in pH 7.4, owing to the disintegration of the metal-ligand bonds within the ZIF frameworks.[24] After 4 h, 22.6% of the loaded DHA in D-ZIF was cumulatively released in pH 6.5, and the cumulative release reached 59.3% and 70.0% after 12 h and 48 h, respectively (Figure 2D). By contrast, the DHA release from the D-ZIF was 30.5% and 42.1% when immersed in pH 7.4 for 12 h and 48 h, respectively. This pH-responsive release mechanism of D-ZIF can ensure drug release in tumor environments and enhance cytotoxicity toward tumor tissues while minimizing side effects under normal physiological conditions. To ensure the therapeutic effectiveness of D-ZIF, it is imperative to maintain their stability. D-ZIF maintained stability without significantly increasing hydro-dynamic diameter and PDI in aqueous solution for 48 h (Figure S3).

Based on the above characterizations, D-ZIF demonstrated consistent size, efficient loading efficiency, and pH-responsive drug release, establishing it as a robust drug delivery system for in vivo applications.

Tumor Cell Inhibition of D-ZIF

We performed cytotoxicity of D-ZIF on sensitive A549 and drug-resistant A549-TAX cells by CCK8 to evaluate the antitumor activity. Both free DHA and D-ZIF presented cytotoxicity on A549-TAX cells. By comparison, D-ZIF showed obviously intensified cytotoxicity than free DHA at the equivalent DHA concentration (Figure 3A and Figure S4). D-ZIF showed dose-dependent cytotoxicity ranging from 1 to 50 μg/mL, which may be ascribed to the enhanced endocytosis of D-ZIF by the rapid cellular uptake and the sustained release of DHA. We hypothesize that the D-ZIF-caused tumor cell cytotoxicity is related to apoptosis. To prove this, we analyzed the apoptosis rate of A549-TAX cells treated by various materials through flow cytometry (FCM) assay. There was no obvious apoptosis in the control and ZIF group. However, apoptotic cells significantly increased in the free DHA and D-ZIF groups. Compared with the free DHA group with 31.75% of apoptosis, the percentage of apoptotic cells was approximately 76.67% in the D-ZIF group (Figure 3B and Figure S5A). The apoptotic proportion gradually elevated (24.30%, 71.20%, and 82.57%) with the increase of the concentration of loaded DHA (1, 5, and 10 μg/mL) (Figure 3C and Figure S5B). We observed a similar phenomenon in glioma and renal cell carcinoma cell lines, confirming the versatility of our system in treating various types of cancers (Figure S6). Furthermore, we stained the cells with acridine orange/ethidium bromide (AO-EB) to observe the morphological change by a fluorescence microscope. In general, normal cells were stained by green fluorescence, while early apoptotic cells were labeled with yellowish and late apoptotic cells exhibited orange-red fluorescence. There were no apoptotic cells in the control and ZIF group, while early-stage apoptotic cells were observed in the DHA group, and the number of late-stage apoptotic cells increased in the D-ZIF group (Figure 3D and Figure S7). Also, treatment with D-ZIF resulted in a considerable decrease in the number of adhered cells, as evidenced by the Live/Dead assay analysis (Figure S8), which is consistent with the AO-EB analysis. In contrast, free DHA caused a little portion of cell death, demonstrating the key role of the ZIF as a carrier to facilitate drug delivery.

We explored whether the tumor cell apoptosis was caused by D-ZIF-induced ROS. We used an oxidation-sensitive fluorescent probe (DCFH-DA) to measure the production of ROS in the D-ZIF-treated A549-TAX cells. DCF fluorescence image demonstrated that D-ZIF produces a large amount of ROS, while free DHA only induced a slight elevation of ROS level (Figure 3E). By contrast, the ZIF and control group showed no detectable DCFH-DA fluorescence, indicating that the D-ZIF can significantly improve the antitumor efficacy of DHA. We also quantitatively analyzed the ROS level by flow cytometry. The ROS production in the D-ZIF-treated A549-TAX cells was approximately more than 10 times in the DHA group (Figure S9). We explored the possible antitumor mechanism of D-ZIF. The Nrf2/HO-1 pathway is crucial in protecting A549-TAX cells against oxidative damage in response to ROS.[42] To clarify the effect of D-ZIF on the Nrf2/HO-1 pathway, we used Western blot analysis to measure the expression of Nrf2 and HO-1 in various treatment groups.
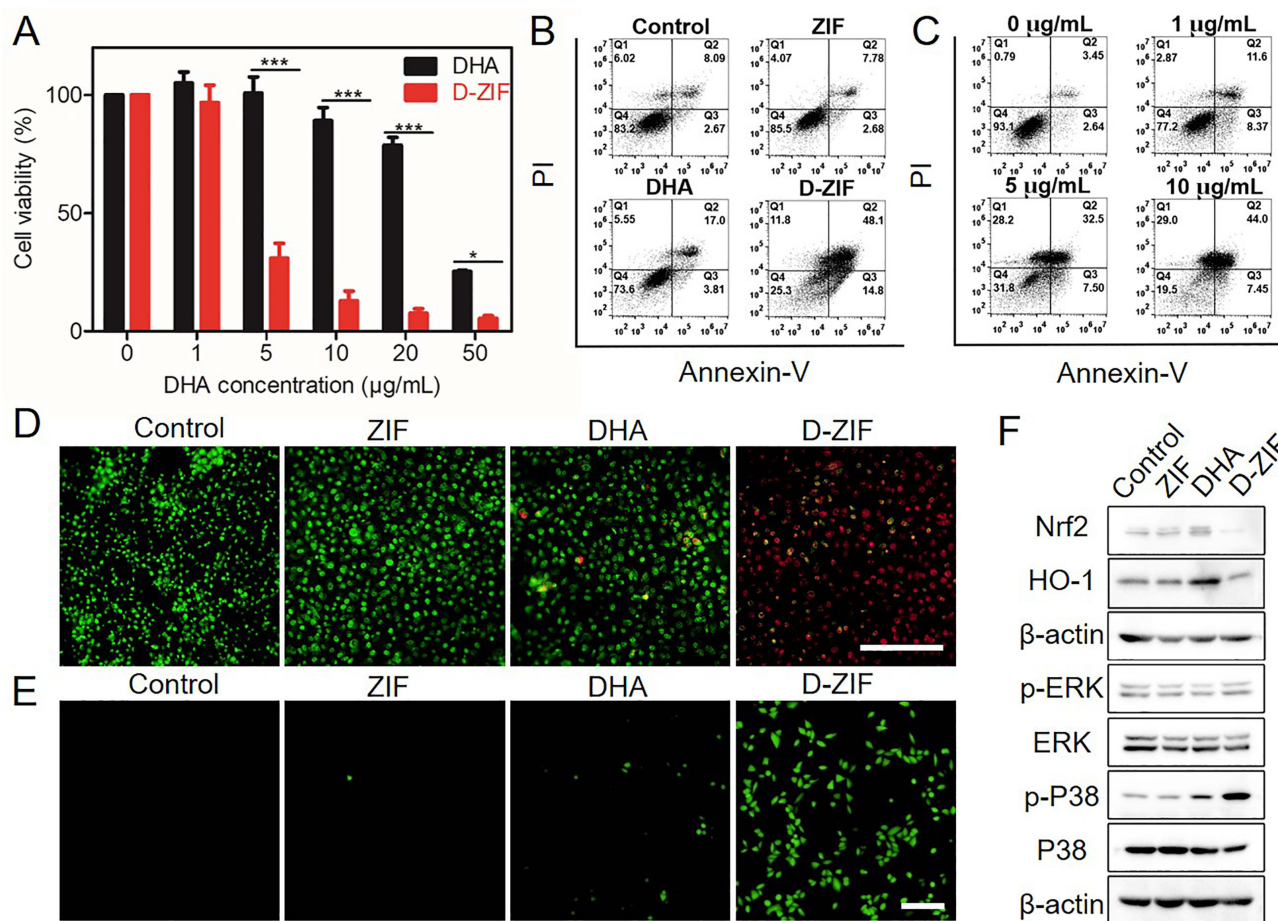
Figure 3 The biological processes induced by various formulations. (**A**) The viability of A549-TAX cells after incubation with different concentration of D-ZIF or free DHA for 24 h. Statistical significance: *p < 0.05, and ***p < 0.001. (**B**) FCM analysis of A549-TAX cells treated with different formulations. (**C**) FCM analyzed data for apoptosis in A549-TAX cells under the treatment of different concentrations of D-ZIF. (**D**) AO-EB dual staining of A549-TAX cells under the treatment of different formulations for 12 h under 20×. Scale bar, 200 μm. (**E**) The ROS levels of A549-TAX cells under the treatment of different formulations are measured by the fluorescent probe. Scale bar, 200 μm. (**F**) A549-TAX cells under the treatment of different formulations to assess the expression on Nrf2/HO-1 and P38 MAPK pathway relative proteins using Western blot.

Compared to the control and ZIF groups, the DHA group exhibited an increased Nrf2 and HO-1 expression, while the D-ZIF group showed a decreased Nrf2 and HO-1 expression, suggesting that this delivery system optimized anti-tumor efficacy of DHA by regulating the Nrf2/HO-1 pathway (Figure 3F and Figure S10). The effective release of DHA modulated the expression level of Nrf2 and HO-1, leading to the maintenance of elevated levels of ROS, which subsequently induced cell apoptosis. The intensively studied mitogen-activated protein kinase (MAPK) pathway is closely associated with the progression of lung cancer progression and is commonly activated in response to stress stimulus. ERK and P38 MAPK (P38) pathways are the main branches of the MAPK pathway, which are stimulated by ROS. As previously reported, the pivotal role of p38 MAPK in ROS-triggered apoptosis of lung cancer cells has been well-established.[43] The WB analysis revealed a sharp up-regulation of p-P38 in the D-ZIF group, whereas there was a little increase of p-P38 in the DHA group compared to the control and ZIF groups (Figure 3F and Figure S11). Thus, D-ZIF can induce tumor cell apoptosis by up-regulation of the P38 MAPK pathway. ROS have the capability to activate Nrf2, resulting in the upregulation of downstream antioxidant enzymes such as HO-1.[44] However, an excessive and rapid generation of ROS can disrupt the redox balance, potentially leading to the deactivation of Nrf2.[45] Moderate ROS induced by DHA triggered Nrf2 activation, initiating the antioxidant mechanism to subsequently decrease ROS levels. Conversely, the excessive ROS induced by D-ZIF hindered the redox mechanism mediated by previously activated Nrf2. Moreover, a more complex generation of ROS could potentially play a role in inhibiting Nrf2, sustaining a detrimental cycle of increasing ROS levels.[45] The increased accumulation of ROS in cancer cells initiated apoptosis by activating diverse apoptotic signaling

pathways,[46,47] with the activated P38MAPK pathway assuming a pivotal role in inducing cell apoptosis.[48] In summary, D-ZIF can effectively regulate the Nrf2/HO-1 expression and maintain a high level of ROS, thus continuously activate P38 MAPK signaling pathways, leading to favorable antitumor effects.

Biocompatibility Evaluation of ZIF Delivery System

We tested the toxicity of ZIF at the cellular level by incubating different concentrations of ZIF with A549-TAX cells. Even at a relatively high concentration (640 μg/mL), ZIF did not exhibit any significant cytotoxicity, indicating its good biocompatibility as a drug delivery carrier (Figure 4A). Additionally, the cells cultured with ZIF displayed spindle and quadrangular shapes like the normal cells, and the cell count in the ZIF delivery system was comparable to that of the control group, which further supports the notion that the ZIF delivery system has minimal negative impact on cell viability (Figure 4B). To assess the biocompatibility of ZIF and D-ZIF in the bloodstream, we performed a hemolysis test. Neither ZIF nor D-ZIF induced any observable hemolysis at high concentrations, even up to 320 μg/mL for ZIF and 50 μg/mL for D-ZIF (Figure 4C). Thus, ZIF and D-ZIF exhibited a wide range of safe concentrations suitable for blood-contacting applications. Consequently, D-ZIF hold great potential for utilization in clinical antitumor application.
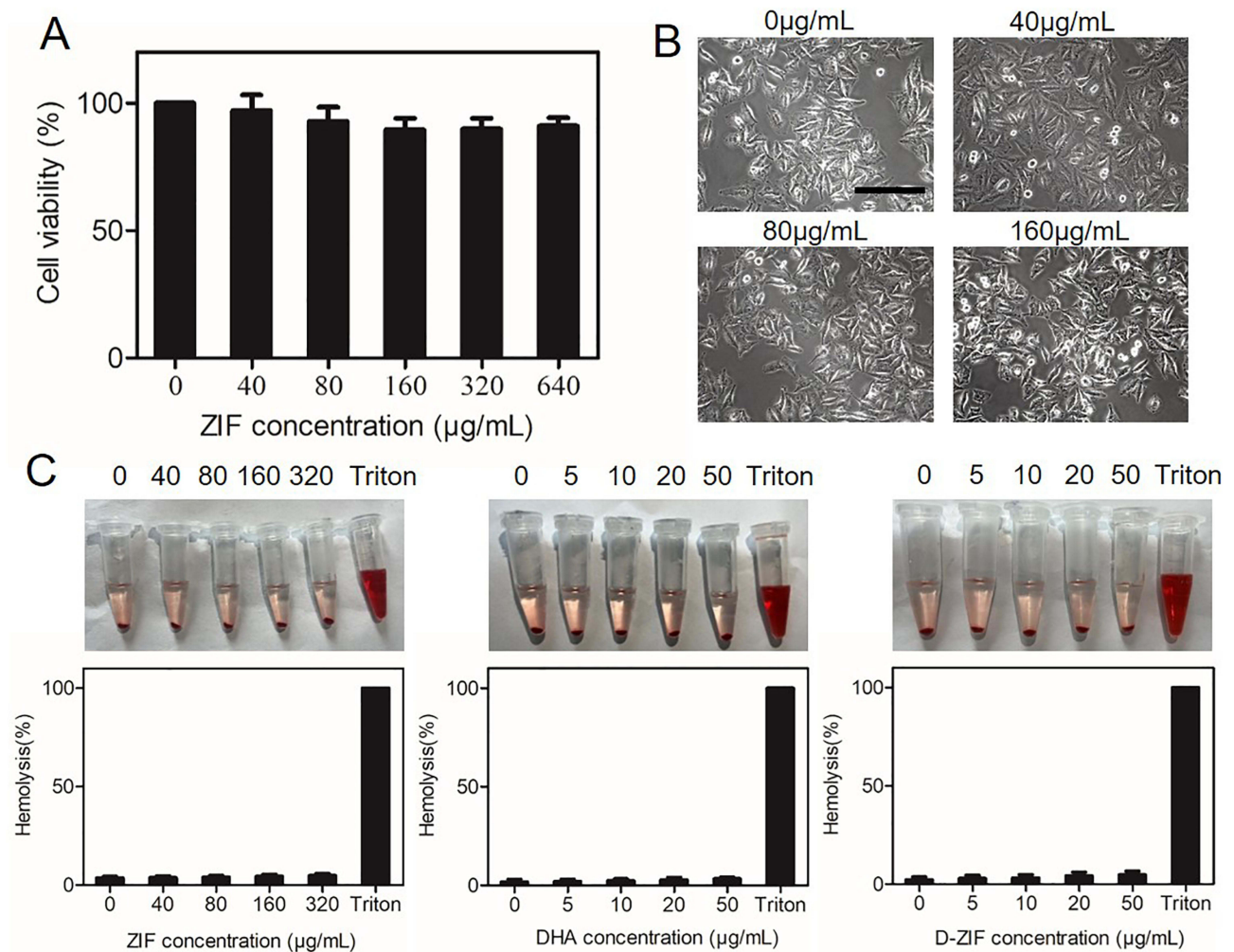

Figure 4 Biocompatibility evaluation of the ZIF delivery system. (**A**) Cell viability of A549-TAX cells under the treatment of different concentrations of ZIF for 24h. (**B**) Images show the states of A549-TAX cells incubated with ZIF. Scale bar, 10 μm. (**C**) The biocompatibility of various concentrations of ZIF, DHA, and D-ZIF is evaluated using rat erythrocytes lysis assay. Saline or triton is utilized as a negative or positive control, respectively. The extent of the cell lysis is quantified by measuring OD_{567nm} for the samples.
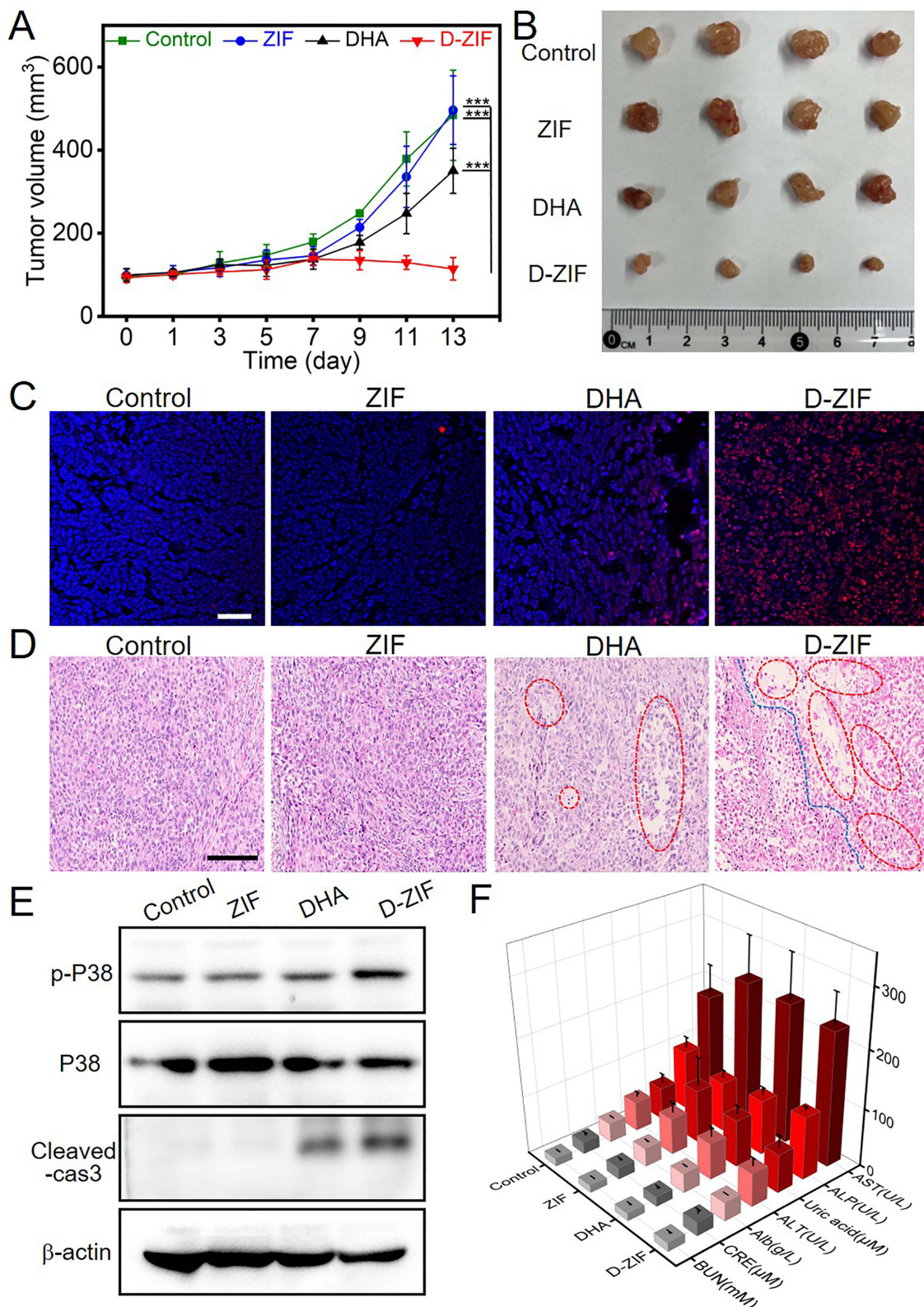
Figure 5 Antitumor activity and mechanism of D-ZIF in the subcutaneous tumor model. (**A**) Tumor growth is monitored and measured at different time points following the different treatments. Statistical analysis revealed a significant difference (n = 6, ***P < 0.001) compared to the D-ZIF group. (**B**) Macroscopic images of the excised tumors in different treatments. (**C**) TUNEL staining is performed on the excised tumor tissue sections to assess apoptotic cell death, Scale bar, 50 μm. (**D**) HE staining of the excised tumor tissue sections. Red circles indicated the tumor cell necrosis and blue line marked the tumor structure disintegrated. Scale bar, 100 μm. (**E**) Western blot of the excised tumors in different treatments. (**F**) The level of different biomarkers indicating liver and kidney function, and nutritional status after different treatments. Between-group changes were assessed using ANOVA with a threshold P=0.05.

Antitumor Activity and Mechanism in vivo

We further explored the in vivo antitumor efficiency and the related mechanism of D-ZIF. Mice were randomly assigned to four groups (n=6), control group (saline), free DHA group, ZIF group, and D-ZIF group with the equivalent DHA doses (100 μg per mice). The relative tumor volume in both the control and ZIF group evidently increased, indicating that ZIF itself has no tumor inhibition effect, while the free DHA group presented a slight inhibition (Figure 5A). On the contrary, the tumor volume and weight of the D-ZIF-treated mice reduced by 76.3% and 79.1% compared to the control group, displaying efficient antitumor efficiency (Figure 5A and B, Figure S12). At the same dose of DHA, D-ZIF showed superior DHA bioavailability for better therapeutic efficacy than the DHA group. In addition, the body weight is stable during the observation period, implying negligible systemic toxicity of D-ZIF (Figure S13). Notably, the D-ZIF remarkably inhibited resistant cells that caused tumor growth.

We further evaluated the antitumor mechanism of D-ZIF by TUNEL staining and Western blot. Compared with the control group, both DHA and D-ZIF caused tumor cell apoptosis (Figure 5C). We excised the tumors for HE analysis (Figure 5D). The tumor structure remained intact with large and hyperchromatic cell nuclei in the control and ZIF groups. Meanwhile, DHA and D-ZIF treatments induced varying levels of cell necrosis and a loose cell arrangement (indicated by red circles). By comparison, a large number of tumor cells died and tumor structure disintegrated in the D-ZIF group (marked by the blue line), indicating the high antitumor efficacy of the delivery system (Figure 5D). D-ZIF treatment simultaneously led to the up-regulation of the P38 MAPK pathway, which may also contribute to the apoptosis (Figure 5E). Furthermore, the treatment with D-ZIF exhibited a significant enhancement in the cleavage of caspase-3, a protein associated with apoptosis. In contrast, there is only a slight increase of p-P38 and cleaved caspase-3 in the DHA group, and no change is observed in the control and ZIF groups (Figure 5E). These results demonstrate that D-ZIF has potent pro-apoptotic effects through the P38 MAPK pathway in vivo.

We also assessed the biocompatibility of the ZIF delivery system by measuring the levels of biochemical biomarkers. The mice treated with D-ZIF maintained the levels of kidney function biomarkers (creatinine, CRE; blood urea nitrogen, BUN and uric acid), liver function biomarkers (aspartate aminotransferase, AST; alanine aminotransferase, ALT and alkaline phosphatase, ALP) and nutritional status (albumin, Alb) within the normal range, indicating the normal functioning of key organs (Figure 5F). We also performed a significance analysis utilizing One-way analysis of variance (ANOVA) with a threshold set at $P=0.05$ for comparisons between each group. There is no significant difference between the control and experimental groups. Together, D-ZIF showed obvious effects in treating tumors with high safety.

Conclusion

In this study, we developed a highly effective drug delivery system using ZIF-8 to deliver DHA for cancer treatment. D-ZIF possessed a noticeable DHA encapsulation efficiency (72.9%) and a smooth release profile triggered by acidic microenvironments in the tumor. This pH-responsive release mechanism enhances the targeting efficiency of DHA towards tumor cells, thereby increasing drug concentration in tumor sites. D-ZIF inhibited tumor growth by inducing tumor cell apoptosis through the mechanism of ROS production and regulation of Nrf2/HO-1 and P38 MAPK signaling pathways. Moreover, the D-ZIF nanoplatform demonstrated minimal side effects. Our study opens doors for further exploration and investigation of safe and effective drug delivery systems for cancer therapy. In our future work, we intend to investigate long-term biodistribution, biotransformation, and bioavailability of the D-ZIF delivery system aiming to advance treatment approaches for various cancer types. Furthermore, it is imperative to evaluate the D-ZIF delivery system in mitigating drug resistance, providing insights for the development of innovative delivery systems.

Abbreviations

DHA, Dihydroartemisinin; ZIF, zeolitic imidazolate framework; D-ZIF, DHA-loaded ZIF; A549-TAX, TAX-resistant human lung adenocarcinoma; ROS, reactive oxygen species; HE, hematoxylin and eosin-stained.

Acknowledgments

Disclosure

The author reports no conflicts of interest in this work.

References

1. Bray F, Ferlay J, Soerjomataram I, Siegel RL, Torre LA, Jemal A. Global cancer statistics 2018: GLOBOCAN estimates of incidence and mortality worldwide for 36 cancers in 185 countries. *Ca a Cancer J Clinicians*. 2018;68(6):394–424. doi:10.3322/caac.21492
2. Jiang D, Shi Y, Qiu Y, et al. A multidimensional biosensor system to guide LUAD individualized treatment. *J Mat Chem B*. 2021;9(38):7991–8002. doi:10.1039/D1TB00731A
3. Shi J, Shiraishi K, Choi J, et al. Genome-wide association study of lung adenocarcinoma in East Asia and comparison with a European population. *Nat Commun*. 2023;14(1):3043. doi:10.1038/s41467-023-38196-z
4. Kaur R, Bhardwaj A, Gupta S. Cancer treatment therapies: traditional to modern approaches to combat cancers. *Molecular Biology Reports*. 2023;50(11):9663–9676. doi:10.1007/s11033-023-08809-3
5. Duan C, Yu M, Xu J, Li B-Y, Zhao Y, Kankala RK. Overcoming cancer multi-drug resistance (MDR): reasons, mechanisms, nanotherapeutic solutions, and challenges. *Biomed. Pharmacother*. 2023;162:114643. doi:10.1016/j.biopha.2023.114643
6. Liu C, Han Y, Kankala R, Wang S, Chen A. Subcellular Performance of Nanoparticles in Cancer Therapy. *Int j Nanomed*. 2020;15:675–704. doi:10.2147/IJN.S226186
7. Kankala RK, Liu C-G, Yang D-Y, Wang S-B, Chen A-Z. Ultrasmall platinum nanoparticles enable deep tumor penetration and synergistic therapeutic abilities through free radical species-assisted catalysis to combat cancer multidrug resistance. *Chem Eng J*. 2020;383:123138. doi:10.1016/j.cej.2019.123138
8. Ma S, Liu J, Li W, et al. Machine learning in TCM with natural products and molecules: current status and future perspectives. *ChinMed*. 2023;18(1):43. doi:10.1186/s13020-023-00741-9
9. Wei D, Yang H, Zhang Y, et al. Nano-traditional Chinese medicine: a promising strategy and its recent advances. *J Mat Chem B*. 2022;10(16):2973–2994. doi:10.1039/D2TB00225F
10. Xu F, Li M, Que Z, et al. Combined chemo-immuno-photothermal therapy based on ursolic acid/astragaloside IV-loaded hyaluronic acid-modified polydopamine nanomedicine inhibiting the growth and metastasis of non-small cell lung cancer. *J Mat Chem B*. 2023;11(15):3453–3472. doi:10.1039/D2TB02328H
11. Sun K, Deng T, Sun J, et al. Ratiometric fluorescence detection of artemisinin based on photoluminescent Zn-MOF combined with hemin as catalyst. *Spectrochim Acta A Mol Biomol Spectrosc*. 2023;289:122253. doi:10.1016/j.saa.2022.122253
12. Tu Y. The discovery of artemisinin (qinghaosu) and gifts from Chinese medicine. *Nature Med*. 2011;17(10):1217–1220. doi:10.1038/nm.2471
13. Tu Y. Artemisinin-A gift from traditional Chinese medicine to the world (Nobel Lecture). *Angewand Chem*. 2016;55(35):10210–10226. doi:10.1002/anie.201601967
14. Augustin Y, Staines HM, Krishna S. Artemisinins as a novel anti-cancer therapy: targeting a global cancer pandemic through drug repurposing. *Pharmacol Ther*. 2020;216:107706. doi:10.1016/j.pharmthera.2020.107706
15. Wang Y, Yuan X, Ren M, Wang Z. Ferroptosis: a new research direction of Artemisinin and its derivatives in anti-cancer treatment. *Am J Chin Med*. 2024;2024:1–21.
16. Li Y, Zhou X, Liu J, et al. Dihydroartemisinin inhibits the tumorigenesis and metastasis of breast cancer via downregulating CIZ1 expression associated with TGF-β1 signaling. *Life Sci*. 2020;248:117454. doi:10.1016/j.lfs.2020.117454
17. Guimarães D, Cavaco-Paulo A, Nogueira E. Design of liposomes as drug delivery system for therapeutic applications. *Int J Pharm*. 2021;601:120571. doi:10.1016/j.ijpharm.2021.120571
18. Liu P, Chen G, Zhang J. A review of liposomes as a drug delivery system: current status of approved products, regulatory environments, and future perspectives. *Molecules*. 2022;27:4.
19. Zhang L, Wang P, Feng Q, et al. Lipid nanoparticle-mediated efficient delivery of CRISPR/Cas9 for tumor therapy. *PG Asia Materials*. 2017;9(10):e441. doi:10.1038/am.2017.185
20. Liu S, Zhou D, Yang J, Zhou H, Chen J, Guo T. Bioreducible Zinc(II)-coordinative polyethylenimine with low molecular weight for robust gene delivery of primary and stem cells. *J Am Chem Soc*. 2017;139(14):5102–5109. doi:10.1021/jacs.6b13337
21. Samal SK, Dash M, Van Vlierberghe S, et al. Cationic polymers and their therapeutic potential. *Chem Soc Rev*. 2012;41(21):7147–7194. doi:10.1039/c2cs35094g
22. Sung YK, Kim SW. Recent advances in polymeric drug delivery systems. *Biomater Res*. 2020;24:12. doi:10.1186/s40824-020-00190-7
23. Liang C, Zhang X, Wang Z, Wang W, Yang M, Dong X. Organic/inorganic nanohybrids rejuvenate photodynamic cancer therapy. *J Mater Chem B*. 2020;8(22):4748–4763. doi:10.1039/D0TB00098A
24. Paunovska K, Loughrey D, Dahlman JE. Drug delivery systems for RNA therapeutics. *Nat Rev Genet*. 2022;23(5):265–280. doi:10.1038/s41576-021-00439-4
25. Zhang L, Li Y, Yu JC. Chemical modification of inorganic nanostructures for targeted and controlled drug delivery in cancer treatment. *J Mater Chem B*. 2014;2(5):452–470. doi:10.1039/C3TB21196G

26. Zhang L, Yang X, Li Y, Zheng W, Jiang XJC. Hollow carbon nanospheres as a versatile platform for co-delivery of siRNA and chemotherapeutics. *Carbon*. 2017;121:S0008622317305420. doi:10.1016/j.carbon.2017.05.084

27. Shen Y, Ma X, Zhang B, et al. Degradable dual pH-and temperature-responsive photoluminescent dendrimers. *Chemistry*. 2011;17(19):5319–5326. doi:10.1002/chem.201003495

28. Horcajada P, Chalati T, Serre C, et al. Porous metal-organic-framework nanoscale carriers as a potential platform for drug delivery and imaging. *Nature Mater*. 2010;9(2):172–178. doi:10.1038/nmat2608

29. Li HL, Eddaoudi MM, O'Keeffe M, Yaghi OM. Design and synthesis of an exceptionally stable and highly porous metal-organic framework. *nature*. 1999;402(6759):276–279. doi:10.1038/46248

30. Wu MX, Yang YW. Metal-organic framework (MOF)-based drug/cargo delivery and cancer therapy. *Adv Mater*. 2017;29(23). doi:10.1002/adma.201606134

31. Yang L, Lin Y, Zhang J, et al. Biomimetic metal-organic frameworks navigated biological bombs for efficient lung cancer therapy. *J Colloid Interface Sci*. 2022;625:532–543. doi:10.1016/j.jcis.2022.06.008

32. Gao P, Chen Y, Pan W, Li N, Liu Z, Tang B. Antitumor agents based on metal–organic frameworks. *Angew Chem*. 2021;133(31):16901–16914. doi:10.1002/ange.202102574

33. Saeb MR, Rabiee N, Mozafari M, Verpoort F, Voskressensky LG, Luque R. Metal–organic frameworks (MOFs) for cancer therapy. *Materials*. 2021;14(23):7277. doi:10.3390/ma14237277

34. L-G L, Yang -X-X, H-Z X, et al. A dihydroartemisinin-loaded nanoreactor motivates anti-cancer immunotherapy by synergy-induced ferroptosis to activate Cgas/STING for reprogramming of macrophage. *Adv Healthcare Mater*. 2023;12(28):2301561. doi:10.1002/adhm.202301561

35. Wan X, Zhong H, Pan W, et al. Programmed release of dihydroartemisinin for synergistic cancer therapy using a CaCO3 mineralized metal-organic framework. *Angew Chem Int Ed*. 2019;58(40):14134–14139. doi:10.1002/anie.201907388

36. Yan Y, Yang X, Han N, et al. Metal-organic framework-encapsulated dihydroartemisinin nanoparticles induces apoptotic cell death in ovarian cancer by blocking ROMO1-mediated ROS production. *J Nanobiotechnol*. 2023;21(1):204. doi:10.1186/s12951-023-01959-3

37. Chen Y, Wang B, Chen W, et al. Co-delivery of dihydroartemisinin and indocyanine green by metal-organic framework-based vehicles for combination treatment of hepatic carcinoma. *Pharmaceutics*. 2022;14(10):2047. doi:10.3390/pharmaceutics14102047

38. Sun Y, Zheng L, Yang Y, et al. Metal-organic framework nanocarriers for drug delivery in biomedical. *Nano-Micro Lett*. 2020;12:103. doi:10.1007/s40820-020-00423-3

39. Jiang X, Zhao Y, Sun S, et al. Research development of porphyrin-based metal-organic frameworks: targeting modalities and cancer therapeutic applications. *J Mat Chem B*. 2023;11(27):6172–6200. doi:10.1039/D3TB00632H

40. Hou Q, Wang L, Xiao F, et al. Dual targeting nanoparticles for epilepsy therapy. *Chem Sci*. 2022;13(43):12913–12920. doi:10.1039/D2SC03298H

41. Bahar E, Kim JY, Kim HS, et al. Establishment of acquired cisplatin resistance in ovarian cancer cell lines characterized by enriched metastatic properties with increased twist expression. *Int J Mol Sci*. 2020;21(20):7613. doi:10.3390/ijms21207613

42. Xu K, Ma J, Hall SRR, Peng RW, Yang H, Yao F. Battles against aberrant KEAP1-NRF2 signaling in lung cancer: intertwined metabolic and immune networks. *Theranostics*. 2023;13(2):704–723. doi:10.7150/thno.80184

43. ArulJothi KN, Kumaran K, Senthil S, et al. Implications of reactive oxygen species in lung cancer and exploiting it for therapeutic interventions. *Med Oncol*. 2022;40(1):43. doi:10.1007/s12032-022-01900-y

44. Arslanbaeva LR, Santoro MM. Adaptive redox homeostasis in cutaneous melanoma. *Redox Biol*. 2020;37:101753. doi:10.1016/j.redox.2020.101753

45. Kasai S, Shimizu S, Tatara Y, Mimura J, Itoh K. Regulation of Nrf2 by mitochondrial reactive oxygen species in physiology and pathology. *Biomolecules*. 2020;10(2):320. doi:10.3390/biom10020320

46. Carmody RJ, Cotter TG. Signalling apoptosis: a radical approach. *Redox Rep*. 2001;6(2):77–90. doi:10.1179/135100001101536085

47. Wang Y, Guo S-H, Shang X-J, et al. Triptolide induces Sertoli cell apoptosis in mice via ROS/JNK-dependent activation of the mitochondrial pathway and inhibition of Nrf2-mediated antioxidant response. *Acta Pharmacol Sin*. 2018;39(2):311–327. doi:10.1038/aps.2017.95

48. Kwak A-W, Kim W-K, Lee S-O, et al. Licochalcone B induces ROS-dependent apoptosis in oxaliplatin-resistant colorectal cancer cells via p38/JNK MAPK signaling. *Antioxidants*. 2023;12(3):656. doi:10.3390/antiox12030656